High Efficiency Three-Coil Wireless Power Transfer for EV Battery Charging Through Negative-Polarity Partial Power Conversion

Muxing Wu, *Graduate Student Member, IEEE*, Io-Wa Iam, and Chi-Seng Lam, *Senior Member, IEEE*

***Abstract*—As electric vehicles (EVs) become increasingly prevalent, the need for efficient wireless charging solutions grows more pressing. Herein, an innovative wireless charging system is proposed for EVs that achieves high efficiency through a negative-polarity partial power conversion (NP-PPC) approach. While conventional PPC methods are constrained by series-connected relationships, our proposed NP-PPC approach inverts the voltage polarity of the dc/dc regulation converter that enables a redesign of power flow paths. This breakthrough allows a significantly larger portion of power to be unregulated, thus substantially improving the overall system efficiency. Moreover, the system implements a novel three-coil loosely-coupled transformer structure that creates two noninterfering power paths that can eliminate the complexity of conventional coil designs. On this basis, a synchronous checking and mode-switching control strategy achieves both constant current and constant voltage charging without wireless communication. Finally, experimental results from a 1200 W prototype demonstrate the system's effectiveness, achieving a peak efficiency of 94.156%.**

***Index Terms*—Cascaded buck-boost (CBB) converters, partial power conversion (PPC), wireless charging system (WCS), wireless power transfer (WPT).**

I. Introduction

With the development of electric vehicle (EV) technology, nonpetroleum-based personal transportation is a potential solution to environmental pollution and energy shortages. However, conventional wired charging solutions susceptible to interface deterioration and even safety hazards within complex charging environments. In contrast, wireless power transfer (WPT) technology offers a swift and effortless operation that can adapt to intricate surroundings while mitigating risks associated with electrical damage or electric shock [1], [2]. Consequently, it is highly suitable for outdoor charging scenarios of EVs, thus establishing wireless charging systems (WCS) has become a research hotspot [4], [5].

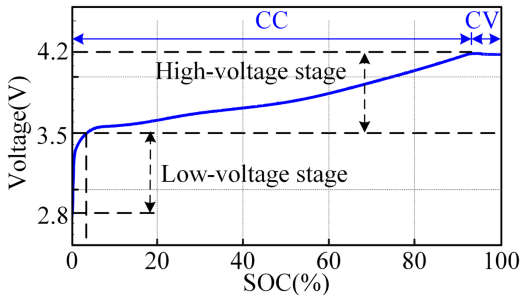

Fig. 1. Voltage-SOC characteristics curve of battery in CC-CV charging.

At present, lithium batteries are commonly employed as power sources for EVs. Along with the development of EV power battery technology, the high-voltage (HV) EV battery charging platform becomes prevalent to enable fast charging, thus necessitating a wide range of voltage regulation in the WCS [6], [7]. Fig. 1 illustrates the voltage—state of charge (SOC) curve of a single lithium battery charged using the constant current and constant voltage (CC-CV) charging profile. During the initial charging stages, battery voltage rises rapidly until reaching a specific threshold and then rises slowly. Subsequently, it enters the CV charging stage until the completion of the charging process [6], [8]. The total charging process is assumed to be divided into stages of HV and low-voltage (LV). In that case, the HV stage constitutes almost of the overall charging process. Therefore, the WCS are required to achieve charging with high transfer efficiency in the HV stage during battery charging. Another issue is that conventional WCSs rely on wireless communication between the transmitter and receiver, which is susceptible to interference from various frequency bands of wireless signals in the outdoor environment [9]. Combining the above concerns, it is necessary to investigate a WCS with a wide output range and high transfer efficiency without wireless communication.

Many compensation topologies have been used as single-stage WCS to charge batteries with CC-CV or other charging

Received 15 August 2024; revised 11 December 2024; accepted 13 January 2025. Date of publication 4 February 2025; date of current version 20 March 2025. This work was supported in part by The Science and Technology Development Fund, Macau SAR (FDCT), under Grant 0050/2024/ITP2, Grant 0015/2022/AMR, Grant 0027/2021/A1, and Grant 004/2023/SKL, and in part by the University of Macau under Grant MYRG-GRG2024-00086-IME and Grant MYRG-GRG2023-00167-IME. Recommended for publication by Associate Editor S. Y. Jeong. *(Corresponding author: Chi-Seng Lam.)*

Muxing Wu and Chi-Seng Lam are with the State Key Laboratory of Analog and Mixed-Signal VLSI, University of Macau, Macau 999078, China, also with the Institute of Microelectronics, University of Macau, Macau 999078, China, and also with the Department of Electrical and Computer Engineering, Faculty of Science and Technology, University of Macau, Macau 999078, China (e-mail: cslam@um.edu.mo, c.s.lam@ieee.org).

Io-Wa Iam is with the State Key Laboratory of Analog and Mixed-Signal VLSI, University of Macau, Macau 999078, China, and also with the Institute of Microelectronics, University of Macau, Macau 999078, China.

Color versions of one or more figures in this article are available at https://doi.org/10.1109/TPEL.2025.3538756.

Digital Object Identifier 10.1109/TPEL.2025.3538756

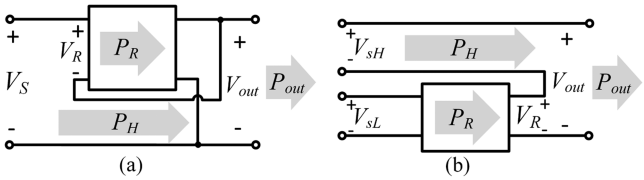

Fig. 2. Conventional PPC structure. (a) Used in [16]. (b) Used in [25].

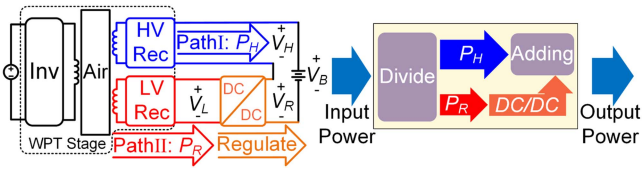

Fig. 3. Connection structure and power flow of the conventional PPC.

profiles, which can be categorized into transmitter control and receiver control methods. Techniques such as phase shift modulation [10], phase frequency modulation [11], switching capacitance control [12], variable inductance control [13] and reconfigurable topology [14] have been proposed to achieve wide voltage range regulation at the transmitter side. However, these methods require wireless communication between transmitter and receiver, making them unsuitable for complex outdoor charging environments. Additionally, an indirect method that estimates the load parameter by sampling and implementing a phase-locked loop on the resonant tank at the transmitter side [9] requires an additional high-frequency current detection circuit to achieve output regulation, resulting in a complex and interference-susceptible control method. Another approach involves incorporating a two-stage circuit at the receiver, where the first stage is responsible for voltage level conversion, and the second stage performs regulation to achieve a wide output voltage range [15]. However, this method sacrifices efficiency as all the power is regulated in two stages.

To reduce power loss caused by regulation, a quasi-single-stage structure based on the concept of partial power conversion (PPC) was introduced in [16] for photovoltaic applications. As shown in Fig. 2(a), the PPC structure allows most of the power (unregulated power, P_H) to flows directly into the load without regulation, while only a small portion (regulated power, P_R) flows into the dc/dc converter for voltage and current regulation. This structure significantly reduces the amount of power to be regulated, improving overall system efficiency. PPC technology has been successfully applied to renewable energy generation, battery storage systems, and other fields [17], [18], [19], [20], [21]. The PPC concept has been introducing into the WCS by [22], as shown in Fig. 2(b), offering lower voltage stress, higher efficiency and higher power density compared with a two-stage circuit. This technique was further explored in [23] and [24], where the WPT stage provided two power transmission paths with noncross-interference. Both [23] and [24] use a double-bipolar structure to eliminate cross-coupling between coils on the same side, thereby establishing two independent power transmission paths. However, these designs required four coils, increasing the design complexity and application cost. To reduce the number of wireless coils, magnetic integrated inductors [25] or a bipolar coil structure [26] were employed. Nevertheless, these approaches introduced additional complexity or reduced the coupling coefficient between transmitter and receiver coils, consequently lowering system efficiency.

In PPC structures, the ratio of P_R to P_H is a critical index for evaluating performance. Previous studies have optimized this ratio; however, P_H is always lower than the output power P_B due to the limitation of the voltage relationship. Furthermore, in battery charging scenarios, achieving a low power ratio necessitates an extremely wide regulation range for the regulation dc/dc converter, which poses challenges in ensuring efficiency under light load conditions. These factors impede conventional PPC theory-based optimization of efficiency. By operating the polarity of the regulating voltage to negative, the concept of negative polarity partial power conversion (NP-PPC) breaks through the voltage relationship limitation in the conventional PPC structure, enabling a higher P_H compared to the output power P_B, thereby enhancing the overall system efficiency.

In this article, a high-efficiency three-coil NP-PPC WCS is proposed. Two power paths without cross-interference are realized by only three coils, with HV side power for load supply and LV side circuit for regulation. The advantages of NP-PPC in terms of efficiency during the battery charging process are analyzed. A 500W experimental prototype is built for verification. Moreover, the main contributions of this article are summarized as follows.

1) The NP-PPC concept is proposed to overcome the limitation of series-connected relationships on HV voltage. Compared to conventional PPC, the NP-PPC approach allows a greater proportion of unregulated power to flow directly into the load, thereby enhancing system efficiency.
2) No decoupling design is required for the receiver coil, and a compact three-coil structure is employed to establish two noncross-interference power paths without, increasing the compactness of the WCS.
3) A communication-free CC-CV control strategy with hysteresis control switching is developed, enhancing the system's adaptability to complex charging environments.

The rest of this article is organized as follows. Section II analyzes the proposed NP-PPC concept and its advantages. Section III describes the three-coil NP-PPC WCS. Section IV presents the overall control strategy without wireless communication. Section V provides experimental verification and efficiency analysis of the proposed system. Finally, Section VI concludes the article.

II. Analysis of Negative-Polarity Partial Power Conversion

A. Conventional Partial Power Conversion Principle

Fig. 3 shows the connection structure of the conventional PPC (i.e., positive polarity partial power conversion, PP-PPC) in WCS. The inverter Inv is located on the transmitter. The HV-Rec and LV-Rec are the rectifiers of the HV side and the LV side. Two power paths P_H and P_R are required to realize the

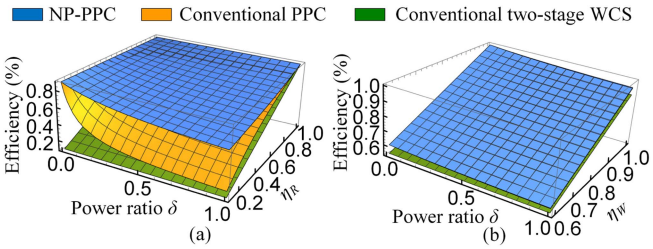

Fig. 4. System efficiency of conventional two-stage WCS, conventional PPC and NP-PPC structures versus power ratios and η_R or η_W. (a) $\eta_W = 0.9$. (b) $\eta_R = 0.9$.

PPC transmission path. The HV-Rec and LV-Rec are located on the receiver. Both outputs of HV-Rec and LV-Rec are designed as constant voltage. The output voltage V_B is the sum of the regulation voltage V_R and the HV voltage V_H. There is the voltage constraint relationship

$$V_H + V_R = V_B. \tag{1}$$

The HV-Rec is directly connected to the load, while the LV-Rec is connected to the input of the dc/dc converter that assumes all regulation functions. According to the PPC principle, the smaller the dc/dc power percentage, the overall system efficiency improves as the percentage of power regulated by the dc/dc converter decreases. This is because a smaller regulated power portion leads to lower power losses associated with the regulation process. Consequently, the following power relationship exists:

$$\delta = \frac{P_R}{P_H} = \frac{V_R}{V_H} < 1. \tag{2}$$

The overall system efficiency can be obtained as

$$\eta_P = \frac{\eta_R \eta_W (1+\delta)}{\eta_R + \delta} \tag{3}$$

where η_W is the transfer efficiency of the WPT stage and η_R is the efficiency of the dc/dc converter. As illustrated in Fig. 4, the yellow surface demonstrates superior efficiency of the conventional PPC compared to the efficiency of the conventional two-stage structure highlighted in green, while the control the power ratio δ remains below 1. However, the smaller δ is, the more pronounced the efficiency enhancement of the PPC structure becomes. The significance of δ lies in its ability to quantify and evaluate the degree of efficiency improvement achieved by the PPC topology in practical applications.

B. Negative-Polarity PPC Efficiency Optimization

In the conventional PPC structure, the polarity of regulation voltage V_R is always positive, as shown in Fig. 3, while the V_H is always lower than V_B. However, by inverting the polarity of V_R, a novel NP-PPC structure can be realized. With the NP-PPC concept, V_H can be higher than V_B at the same V_R voltage value. This characteristic enables a smaller δ value, which indicates a greater proportion of unregulated power flowing directly into the load, leading to improved system efficiency.

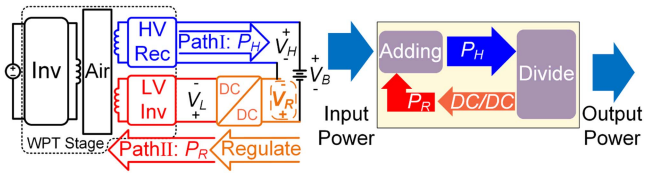

Fig. 5. Connection structure and power flow of the proposed NP-PPC structure.

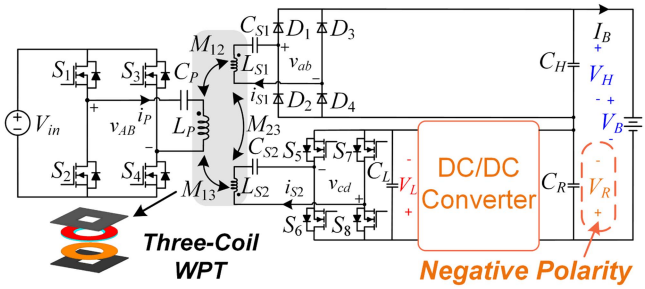

Fig. 6. Proposed three-coil NP-PPC wireless charging system.

In the proposed NP-PPC structure, the power flow of P_R is reversed, and its voltage relationship becomes

$$V_H - V_R = V_B. \tag{4}$$

In this case, V_H will be higher than V_B, and its power flow is indicated by the arrow in Fig. 5. The LV-Inv is the inverter of the LV side. The LV power flows to the HV through the wireless coils. Therefore, during the coil design process, it is crucial to minimize the gap between the LV and HV coils to achieve a coupling coefficient close to 1, thereby mitigating power losses.

Assuming that the power loss transferred from the LV to the HV is negligible, the overall efficiency of the NP-PPC structure can be calculated as

$$\eta_N = \frac{\eta_W (P_H - P_R)}{P_H - P_R \eta_R} = \frac{\eta_W (1-\delta)}{1 - \eta_R \delta}. \tag{5}$$

C. Proposed Three-Coil NP-PPC Wireless Charging System

The proposed three-coil NP-PPC WCS is presented in Fig. 6. L_P, L_{S1} and L_{S2} are the transmitter coil, the receiver coil, and the LV transmitter coil, respectively. C_P, C_{S1}, and C_{S2} form a S/S/S compensation structure. The inverter on the transmitter side is formed by switches S_1-S_4. On the receiver side, a rectifier circuit for the HV-Rec is formed by diodes D_1-D_4, and another inverter circuit for the LV-Inv is formed by switches S_5-S_8. C_H, C_L, and C_R are the filter capacitors of HV-Rec, LV-Inv and dc/dc converter, respectively.

To enhance the coupling coefficient and consequently improve efficiency, L_{S1} and L_{S2} are positioned as closely as possible. During the charging process, power flows from the L_P to L_{S1}. After rectification, the majority of the power is directed to charge the power battery, while a small portion is fed back to L_{S1} through the dc/dc converter and LV-Inv circuit via L_{S2}. The dc/dc converter handles all regulation functions within the system. A detailed analysis of each part will be provided in Section III.

D. Efficiency Comparative Analysis

To facilitate a more intuitive comparison of the efficiency between conventional PPC and NP-PPC, the following comparative analysis will be conducted under the specified conditions.

Figs. 3 and 5 illustrate the power flow direction of the conventional PPC structure and the proposed NP-PPC structure, respectively. To do a fair theoretical comparison, both the terminal voltages of the dc/dc converter V_R and V_L are defined as the same in the conventional PPC and the NP-PPC structures, respectively. According to the NP-PPC concept, the V_H will be higher than the output voltage V_B, creating a lower value of δ, denoted as δ'

$$\delta' = \frac{V_R}{V_H} = \frac{V_R}{V_B + V_R}. \tag{6}$$

Combining (1), (2) and (7), the relationship between δ and δ' can be obtained as

$$\delta' = \frac{\delta}{2\delta + 1}. \tag{7}$$

Substituting (6) gives the system efficiency of the NP-PPC

$$\eta_N = \frac{\eta_W (1 - \delta')}{1 - \eta_R \delta'} = \frac{\eta_W (\delta + 1)}{(2 - \eta_R)\delta + 1}. \tag{8}$$

The efficiency disparity between the conventional PPC and NP-PPC can be determined as

$$\Delta\eta = \eta_N - \eta_P = \frac{\delta\eta_W (1 + \delta)(1 - \eta_R)}{[(2 - \eta_R)\delta + 1](\eta_R + \delta)} > 0. \tag{9}$$

Given that η_R is a constant value and $\eta_R < 1$, it is imperative for (9) to be greater than zero. It can indicate that the system efficiency of the NP-PPC is always higher than the conventional PPC system under the same output voltage V_B and the port voltages of the dc/dc converter V_R and V_L.

Moreover, the system efficiency advantage of the NP-PPC is depicted by the blue surface in Fig. 4. In this comparative analysis, the transfer efficiency of the WPT stage is assumed as a constant $\eta_W = 0.9$, as shown in Fig. 4(a), and the voltage range of V_R is the same with η_R set to 0.9, as shown in Fig. 4(b). These values can be substituted into (3) and (8) to obtain the theoretical efficiency of the whole battery charging process across the specified voltage range. The efficiency of NP-PPC is observed to be higher than that of the conventional PPC and conventional two-stage WCS across various conditions.

Fig. 7(a) illustrates the battery voltage, efficiency, and power ratio versus the charge state. At the beginning of the charging process, the conventional PPC exhibits a lower δ value compared to NP-PPC due to the low battery voltage, resulting in higher efficiency for conventional PPC in the initial stage. By examining the battery voltage curve (blue line) in Fig. 7(a), it can be observed that during the initial stage of charging, the battery voltage rapidly increases to approximately 330 V (V_{B1}), after which the voltage rise becomes more gradual until the completion of charging. V_{B1} roughly corresponds to the critical point separating the LV and HV stages depicted in Fig. 1. When the charging voltage is below V_{B1}, the conventional PPC operates within its efficiency dominant area, constituting only a small portion of the overall charging process. Conversely, once

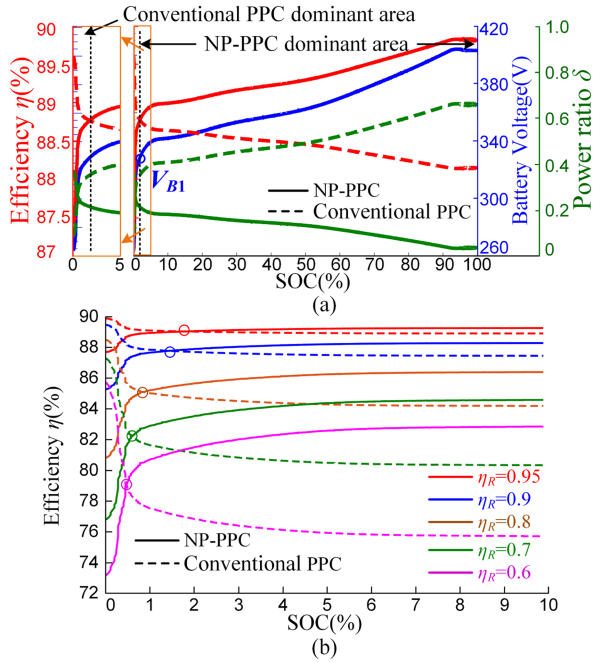

Fig. 7. Comparison of NP-PPC and conventional PPC under (a) overall charging cycle and (b) different η_R.

the charging enters the HV stage, the NP-PPC demonstrates higher efficiency than the conventional PPC and maintains an ever-widening gap until the completion of charging. Furthermore, the NP-PPC also surpasses the conventional PPC at the peak efficiency points.

Fig. 7(b) illustrates the efficiency versus the charge state under various η_R. The superiority of NP-PPC over the conventional PPC in most battery charging cycles is evident, particularly under varying η_R. Furthermore, as the η_R decreases, the crossover point of its efficiency curve gradually advances, and the efficiency difference gradually increases in the HV stage. These observations indicates that the conventional PPC is more sensitive to the efficiency change of dc/dc converters and necessitates the use of more efficient dc/dc converters.

III. Three-Coil NP-PPC Wireless Charging System

A. Three-Coil T-Equivalent Model

As depicted in Fig. 5, the PPC structure contains two power paths, P_H and P_R, to facilitate power division and requires WPT converter to achieve two constant voltage outputs (V_H and V_L) with no cross-interference. The conventional approach utilizes two separate groups of coils to realize the two power paths flow design [24]. However, practical space limitations necessitate coil stacking, which inevitably leads to undesired cross-coupling and thus complicates the coil design.

To circumvent the aforementioned issues, a T-equivalent circuit decoupling model for a three-coil transformer is deduced in this section.

For the three-coil transformer, mutual flux coupling is illustrated in Fig. 8(a), with six inductances, L_1, L_2, L_3, M_{12}, M_{13}

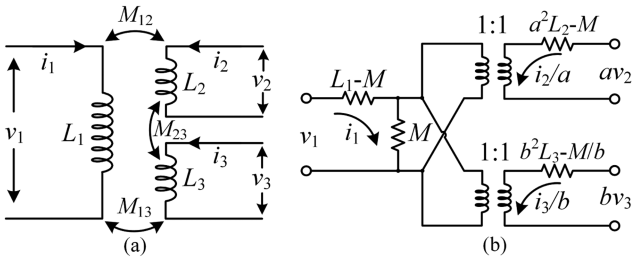

Fig. 8. Three-coil transformer model. (a) Mutual flux coupling. (b) T-equivalent circuit.

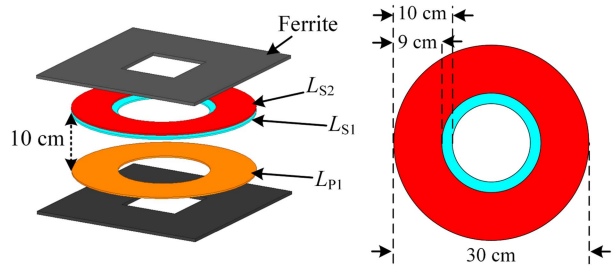

Fig. 9. Three-coil winding of the proposed system.

and M_{23}, where L_1, L_2, and L_3 are self-inductance, M_{12}, M_{13} and M_{23} are mutual inductance.

Applying Kirchhoff's voltage law to coil gives

$$v_1 = L_1 p i_1 + M_{12} p i_2 + M_{13} p i_3 \tag{10}$$

$$v_2 = M_{12} p i_1 + L_2 p i_2 + M_{23} p i_3 \tag{11}$$

$$v_3 = M_{13} p i_1 + M_{23} p i_2 + L_3 p i_3 \tag{12}$$

where $p = d/dt$

$$v_1 = L_1 p i_1 + a M_{12} p\,(i_2/a) + b M_{13} p\,(i_3/b) \tag{13}$$

$$a v_2 = a M_{12} p i_1 + a^2 L_2 p\,(i_2/a) + ab M_{23} p\,(i_3/b) \tag{14}$$

$$b v_3 = b M_{13} p i_1 + ab M_{23} p\,(i_2/a) + b^2 L_3 p\,(i_3/b) \tag{15}$$

where $a \neq 0$ and $b \neq 0$.

Choose

$$a M_{12} = b M_{13} = ab M_{23} = M. \tag{16}$$

From which

$$a = M_{13}/M_{23} \tag{17}$$

$$b = M_{12}/M_{23} \tag{18}$$

$$M = M_{12} M_{13}/M_{23}. \tag{19}$$

The equation then simplified to

$$v_1 = L_1 p i_1 + M p\,(i_2/a) + M p\,(i_3/b) \tag{20}$$

$$a v_2 = M p i_1 + a^2 L_2 p\,(i_2/a) + M p\,(i_3/b) \tag{21}$$

$$b v_3 = b M_{13} p i_1 + ab M_{23} p\,(i_2/a) + b^2 L_3 p\,(i_3/b)\,. \tag{22}$$

Then, the T-equivalent circuit of the three-coil transformer can be obtained as shown in Fig. 8(b), in which there are only four inductor branches and no mutual inductive coupling between inductors.

B. Three-Coil S/S/S Compensation Structure With Two Constant Voltage Outputs

To achieve constant voltage for both the HV-Rec and LV-Inv sides, S/S/S compensation is employed, as illustrated in Fig. 6. However, C_p, C_{s1}, and C_{s2} can be calculated by

$$\omega = \frac{1}{\sqrt{(L_P - M)\,C_P}} = \frac{1}{\sqrt{\left(L_{S1} - \frac{M}{a^2}\right) C_{S1}}} = \frac{1}{\sqrt{\left(L_{S2} - \frac{M}{b^2}\right) C_{S2}}} \tag{23}$$

where $\omega = 2\pi f_w$ is the WPT resonant angular frequency, f_w is the operating frequency of Inv and LV-Inv side.

The voltage relationship can be obtained as

$$V_H = V_{\text{in}} \frac{M_{23}}{M_{13}} \tag{24}$$

$$V_L = V_{\text{in}} \frac{M_{23}}{M_{12}} \tag{25}$$

where M_{12}, M_{13}, M_{23}, respectively, are mutual inductance of L_P to L_{S1}, L_P to L_{S2}, L_{S2} to L_{S1}. From (24) and (25), it can be observed that the output voltage V_H and V_L are two constant voltage outputs independent of the load and are solely determined by the mutual inductance.

The coil structure utilized in the proposed NP-PPC WCS is illustrated in Fig. 9. It consists of one coil L_P on the transmitter side and two coils L_{S1} and L_{S2} on the receiver side, where L_{S1} serves as the receiver coil for the HV-Rec side, and L_{S2} acts as the LV-Inv coil on the receiver side. As power flows from LV-Inv to HV-Rec, it is crucial to position L_{S1} and L_{S2} coils in close proximity to enhance their coupling coefficient. To ensure a relatively high mutual inductance coefficient between L_P and L_{S1}, it is recommended to place L_{S1} between L_P and L_{S2}.

In order to improve the transfer efficiency, it is imperative to implement ZVS turn-ON for Inv, and the ZVS condition can be obtained as

$$\frac{M_{23} V_{\text{in}}}{4 f_w M_{12} M_{13}} \geq 4 C_{\text{oss}} \frac{V_{\text{in}}}{T_d} \tag{26}$$

where C_{oss} is the body capacitance of the MOSFET and T_d is the switching dead time.

The loosely coupled transformer leakage inductance model can eliminate cross-coupling and reduce the number of coils required, resulting in a three-coil WPT structure that can achieve two load-independent constant voltage outputs V_H and V_L without cross-interference.

C. Regulation DC/DC Converter Design

To fulfill the battery charging, PPC structures typically necessitate a wide output range of dc/dc regulation converter. Cascaded buck-boost (CBB) converters are commonly employed in energy transfer systems and offer a wider regulation range compared to conventional buck, boost or buck-boost circuits.

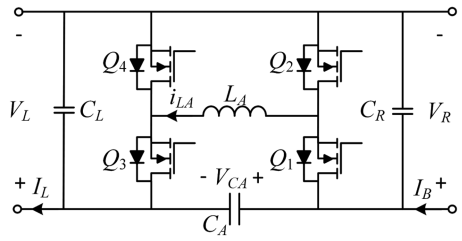

Fig. 10. Cascaded buck-boost converter topology.

TABLE I
SWITCHES OPERATING STATE

Type of operation	Switches state			
	Q_1	Q_2	Q_3	Q_4
Buck	D	1-D	1	0
Buck-Boost	D	1-D	1-D	D
Boost	1	0	1-D	D

The resonant structure formed by the inductor and parasitic capacitors can be meticulously designed to achieve ZVS during the discontinuous conduction mode (DCM), ensuring enhanced transfer efficiency. Auxiliary capacitors are utilized to mitigate output ripple.

The topology of the CBB is shown in Fig. 10, which consists of an auxiliary capacitor C_A, two filter capacitors (C_D, C_L), four switches (Q_1, Q_2, Q_3, Q_4) and an inductor (L_A). By operating the four switches in DCM mode, voltage conversion and ZVS turn-ON can be achieved. The converter operates at a fixed switching frequency, while the voltage gain is adjusted by varying the duty cycle. The switching states are given in Table I.

1) Buck Mode: During buck mode, Q_3 is turned-ON, Q_4 is turned-OFF, with Q_1 and Q_2 engaged in switching operation. The ratio of V_L and V_R can be obtained from the volt-second balance law for L_A, given as

$$\frac{V_L}{V_R} = D \tag{27}$$

where D is the duty cycle.

In order to achieve ZVS turn-ON in DCM mode, it is necessary for the minimum value of i_{LA} to be less than 0, and L_A should be satisfied

$$L_A < \frac{(V_R - V_L)\, DT_s}{2I_{L\max}} \tag{28}$$

where T_s is the switching period of the dc/dc.

The auxiliary capacitance C_a shall be satisfied

$$C_A < \frac{V_L\,(1-D)\,T_s^2}{8L_A\Delta_{\mathrm{VL,ripple}}} - C_L. \tag{29}$$

2) Buck-Boost Mode: During buck-boost mode, all switches are engaged in switching operation. The ratio of V_L and V_R can be obtained from the volt-second balance law for L_A, given as

$$\frac{V_L}{V_R} = \frac{D}{1-D}. \tag{30}$$

TABLE II
POWER LOSS MODEL

Component	Type	Switches state
Inv	Conduction losses	$2I^2_{P,\,rms}\cdot R_{ds(on)}$
Loosely coupler	Copper losses	$(I_{P,\,rms})^2\cdot R_P+(I_{S1,\,rms})^2\cdot R_{S1}+(I_{S2,\,rms})^2\cdot R_{S2}$
	Core losses	$P_{cv,\,P}\cdot V_{e,\,P}+P_{cv,\,S}\cdot V_{e,\,S}$
HV-Rec	Conduction losses	$2(V_f\cdot I_B)$
LV-Inv	Conduction losses	$2I^2_{S2,\,rms}\cdot R_{ds(on)}$
CBB in buck mode	Conduction losses	$2\left(I_L^2+\frac{(V_R-V_L)\cdot D}{12L_A\cdot f_s}\right)\cdot R_{ds(on)}$
	Copper loss of L_A	$\left(I_L^2+\frac{(V_R-V_L)\cdot D}{12L_A\cdot f_s}\right)\cdot R_{LA}$
	Core loss of L_A	$P_{cv,\,LA}\cdot V_{e,\,LA}$
CBB in boost mode	Conduction losses	$2\left(I_R^2+\frac{V_R\cdot D}{12L_A\cdot f_s}\right)\cdot R_{ds(on)}$
	Copper loss of L_A	$\left(I_R^2+\frac{V_R\cdot D}{12L_A\cdot f_s}\right)\cdot R_{LA}$
	Core loss of L_A	$P_{cv,\,LA}\cdot V_{e,\,LA}$
CBB in buck-boost mode	Conduction losses	$2\left((I_R+I_L)^2+\frac{V_R\cdot D}{12L_A\cdot f_s}\right)\cdot R_{ds(on)}$
	Copper loss of L_A	$\left((I_R+I_L)^2+\frac{V_R\cdot D}{12L_A\cdot f_s}\right)\cdot R_{LA}$
	Core loss of L_A	$P_{cv,\,LA}\cdot V_{e,\,LA}$

To achieve ZVS turn-ON, L_A should be satisfied

$$L_A < \frac{V_R DT_s}{2\,(I_{B\max}+I_{L\max})}. \tag{31}$$

The auxiliary capacitance C_a shall be satisfied

$$C_A > \frac{(I_B L_A + V_R DT_s/2)^2}{2L_A\Delta_{\mathrm{VL,ripple}}V_L} - C_L. \tag{32}$$

3) Boost Mode: During boost mode, Q_1 is turned-ON, Q_2 is turned-OFF, with Q_3 and Q_4 engaged in switching operation. The ratio of V_L and V_R can be obtained from the volt-second balance law for L_A, given as

$$\frac{V_L}{V_R} = \frac{1}{1-D}. \tag{33}$$

To achieve ZVS turn-ON, L_A should be satisfied

$$L_A < \frac{V_R DT_s}{2I_{B\max}}. \tag{34}$$

The auxiliary capacitance C_a shall be satisfied

$$C_A > \frac{[2L_A\,(I_B - I_L) + V_R DT_s]^2}{4L_A\Delta_{\mathrm{VL,ripple}}\,(V_L - V_R)} - C_L. \tag{35}$$

D. Power Loss Analysis

The power loss of the proposed three-coil NP-PPC WCS can be divided into the following parts: transmitting inverter (Inv), loosely coupled transformer, receiving high-voltage rectifier (HV-Rec), low-voltage inverter (LV-Inv) and dc/dc converter. The power loss model of the NP-PPC WCS is given in Table II, due to the ZVS turn-ON achieved in Inv, the switching loss can be ignored for simplicity.

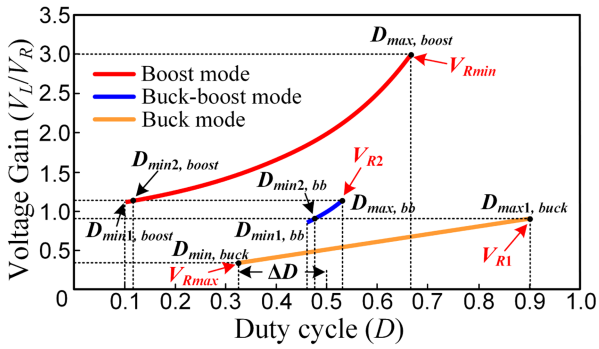

Fig. 11. DC/DC control logic diagram.

Where $R_{\mathrm{ds(on)}}$ is the ON-state resistance, R_P, R_{S1}, and R_{S2} is the coil resistance of L_P, L_{S1}, L_{S2}. $P_{cv,P}$, $P_{cv,S}$, $P_{cv,LA}$ is the core loss per unit volume (kW/m^3) of the transmitter, receiver and L_A, $V_{e,P}$, $V_{e,S}$, $V_{e,LA}$ is the core volume of the transmitter, receiver and L_A, V_f is the forward voltage drop of D_1 to D_4.

IV. Communication-Free Control Strategy and Loss Analysis

In practical applications, the charging environment can be complex, while the charging process needs to be continuous and stable. Therefore, it is imperative to investigate a communication-free control strategy that ensures steady performance.

A. DC/DC Operation Controller Design

In the proposed NP-PPC WCS, a lower δ leads to higher efficiency. However, it imposes stringent requirements on the output capacity of the dc/dc converter. To address variations in V_H and V_R at low δ while maintaining high efficiency, it is necessary for the dc/dc converter to switch between three modes and maintain a reasonable duty cycle. Nevertheless, frequent mode transitions can introduce instability to the system. Therefore, proposing a control strategy that enables hysteresis control switching at different gains while ensuring high efficiency is essential (see Fig. 11). The overall control strategy for transitioning between dc/dc operation modes is described as follows.

1) Buck Mode Operation: The determination of the relationship between battery voltage and duty cycle during the initial charging phase is crucial to ensure symmetrical operation of both buck and boost modes, thereby minimizing inefficient operating. ΔD can be obtained as

$$\Delta D = 0.5 - \sqrt{\frac{V_{R\min}}{V_{R\max}}} \tag{36}$$

where V_{Rmax} is the maximum value of the V_R, and V_{Rmin} is the minimum value of the V_R.

The rated value of V_L can be obtained as

$$V_L = V_{R\max}\left(0.5 - \Delta D\right). \tag{37}$$

The charging process commences with an initial duty cycle of 0.5-ΔD, gradually increasing as the charging progresses. In buck circuits, higher duty cycles result in lower inductor circulation time and enhanced efficiency. Consequently, a maximum duty cycle of $D_{\mathrm{max1,\ buck}} = 0.9$ is determined for buck mode, and once D reaches $D_{\mathrm{max1,\ buck}}$, it transitions into buck-boost mode.

2) Transition From Buck Mode to Buck-Boost Mode: The transition from buck mode to buck-boost mode occurs at V_{R1}, where $D = D_{max1,buck}$. For buck-boost mode, the duty cycles of Q_1, Q_2, Q_3 and Q_4 are D, 1-D, 1-D and D, respectively. During the transition, the D will drop from $D_{\mathrm{max1,\ buck}}$ to $D_{\mathrm{min2,\ }bb}$. Meanwhiles, to ensure the conversion of the buck-boost mode during the transition, a certain margin is reserved as $D_{\mathrm{min1,\ }bb}$

$$V_{R1} = V_L/0.9. \tag{38}$$

3) Buck-Boost Mode Operation: The duty cycle gradually increases during the charging process after entering the buck-boost mode. Due to the requirement of all switches participating in its operation, the efficiency of the buck-boost mode is comparatively lower than that of both buck and boost modes. Consequently, efforts have been made in this design to minimize the operation proportion of the buck-boost mode. When the battery voltage reaches V_{R2}, the transition to boost mode begins.

4) Transition From Buck-Boost Mode to Boost Mode: The transition from buck-boost mode to boost mode occurs at V_{R2}, with $D = D_{\mathrm{max,\ }bb}$. For boost mode, Q_1, Q_2, Q_3, and Q_4 have duty cycles of 1, 0, 1-D, and D, respectively. Currently, the duty cycle will decrease to $D_{\mathrm{min2,\ boost}}$. Similar to buck mode, in boost mode, the smaller the duty cycle, the less the circulation time through the L_A and the higher its efficiency. Therefore, $D_{\mathrm{min1,\ boost}} = 0.1$ is determined as the minimum duty cycle for boost mode

$$V_{R2} = V_L/(1 - D_{\mathrm{min,\ boost}}). \tag{39}$$

5) Boost Mode Operation: After transitioning to boost mode, the duty cycle gradually increases throughout the charging process until it reaches $D = 0.5 + \Delta D$, ultimately completing the charging process.

B. Synchronization Strategy of the Transmitter and Receiver Without Communication

In the proposed NP-PPC WCS structure, the regulation power flow is reversed with a small portion of power being returned from the LV-Inv side to the HV-Rec side. In this article, a synchronous driver signal is generated for the LV-Inv by detecting zero-crossing of i_{s1}, ensuring synchronization between the LV-Inv and Inv side.

The control block diagram of the proposed charging system is illustrated in Fig. 12. The control strategy calculates the load resistance to determine the battery charging stage (CC or CV), and the voltage gain from V_B to determine the dc/dc converter's operating mode (buck, buck-boost, or boost). A simple PI comparator rectifies deviations between feedback and reference values, generating a pulsewidth modulation signal for controlling the dc/dc converter. No wireless communication is required as the transmitter and receiver operate at a fixed frequency f_w.

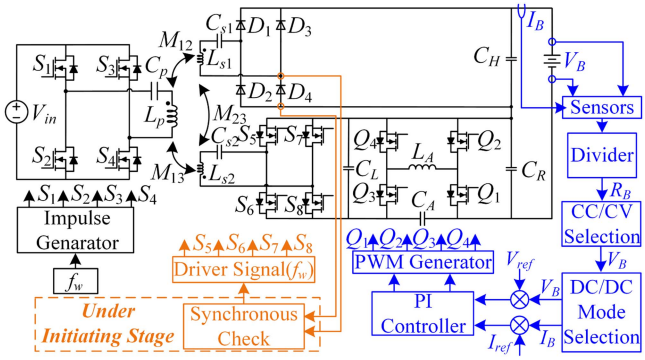

Fig. 12. Control diagram of the proposed charging system.

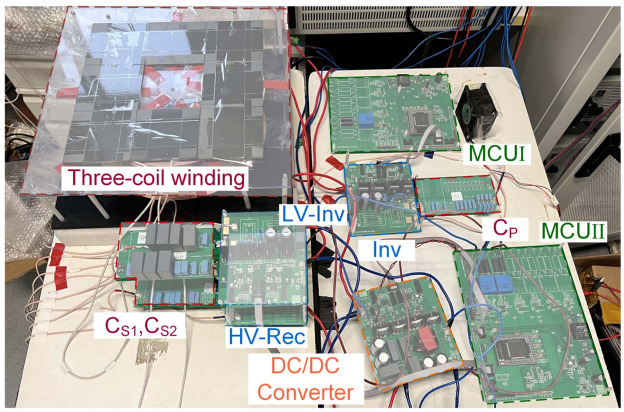

Fig. 13. Experimental prototype.

TABLE III
SPECIFICATIONS OF THE ACTUAL WCS BASED EV AND THE SCALED-DOWN EXPERIMENTAL PROTOTYPE

Parameters	Actual	Scaled-down
Battery pack voltage	250–400 V	264–402 V
Charging power	7.7 kW	1.2 kW
Operating frequency	81.38–90 kHz	85 kHz

V. EXPERIMENTAL VERIFICATION

To validate the CC-CV charging capability of the proposed three-coil NP-PPC WCS without wireless communication, a 1200 W experimental prototype was built in the laboratory, as shown in Fig. 13. To facilitate a direct comparison between the actual WCS based EV (as defined by SAEJ2954 standard) and the proposed scaled-down experimental prototype, relevant parameters are presented in Table III [27], [28]. The corresponding charging specifications involved in the experiment are given in Table IV. For this experiment, an electronic load with resistance range of 88 to 1340 Ω was utilized to simulate the battery. Specifically, the resistance range of 88 to 134 Ω represents the CC charging stage while the resistance range of 134 to 1340 Ω represents the CV charging stage. The configuration of the experimental prototype is given in Table V. The coil structure is consistent with Fig. 9, which is made of 0.07 mm, 714 strands of litz wire.

TABLE IV
CHARGING SPECIFICATIONS

System Specifications, Symbols	Values
Input voltage, V_{in}	140 V
Output voltage range, V_B	264–402 V
HV voltage, V_H	418 V
LV voltage, V_L	50 V
Regulation voltage range, V_R	16–154 V
Rated charging current, $I_{B\max}$	3 A
Minimum charging current, $I_{B\min}$	0.3 A
DC/DC power range	4.8–462 W
Rated charging power	1206 W

TABLE V
EXPERIMENTAL PROTOTYPE PARAMETERS

Parameters, Symbols	Values
WPT Stage Parameters	
Self-inductances, L_P	407.1 μH
Self-inductances, L_{S1}, L_{S2}	384.7 μH, 9.3 μH
Mutual inductance, M_{12}	121.4 μH
Mutual inductance, M_{13}	14.9 μH
Mutual inductance, M_{23}	45.3 μH
Compensation capacitor, C_P	9.5 nF
Compensation capacitors, C_{S1}, C_{S2}	224.4 nF, 941.4 nF
Filter capacitances, C_H	300 μF
DC/DC Converter Parameters	
Operating frequency, f_s	150 kHz
Inductance, L_A	10 μH
Auxiliary capacitance, C_A	30 μF
Input capacitance, C_R	300 μF
Output capacitance, C_L	300 μF

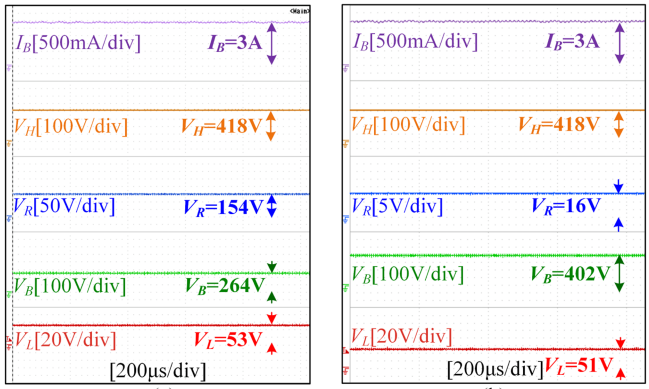

Fig. 14. Steady-state experimental waveforms of the proposed NP-PPC WCS. (a) CC stage. (b) CV stage.

A. Operating Steady-State Waveforms in Charging Process

The steady-state waveform of the system in the CC charging stage is shown in Fig. 14(a) when the power ratio δ is about 0.37, with a battery resistance R_B of 88 Ω. At the beginning of charging, the output voltage V_B is 264 V, maintaining a constant charging current of 3 A. Additionally, the dc/dc converter operates in buck mode with the regulation voltage V_R of 154 V. Fig. 14(b) illustrates the steady-state waveform of the system during the CV charging stage, with δ around 0.038 and an R_B resistance of 134 Ω. The output voltage V_B measures 402 V, while the dc/dc operates in the boost mode with the

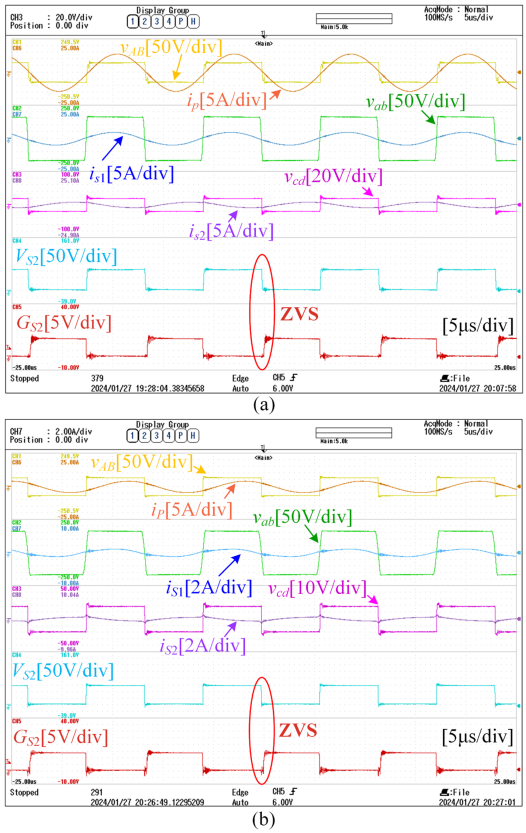

Fig. 15. Measured operating waveforms of the WPT stage. (a) CC charging stage. (b) CV charging stage.

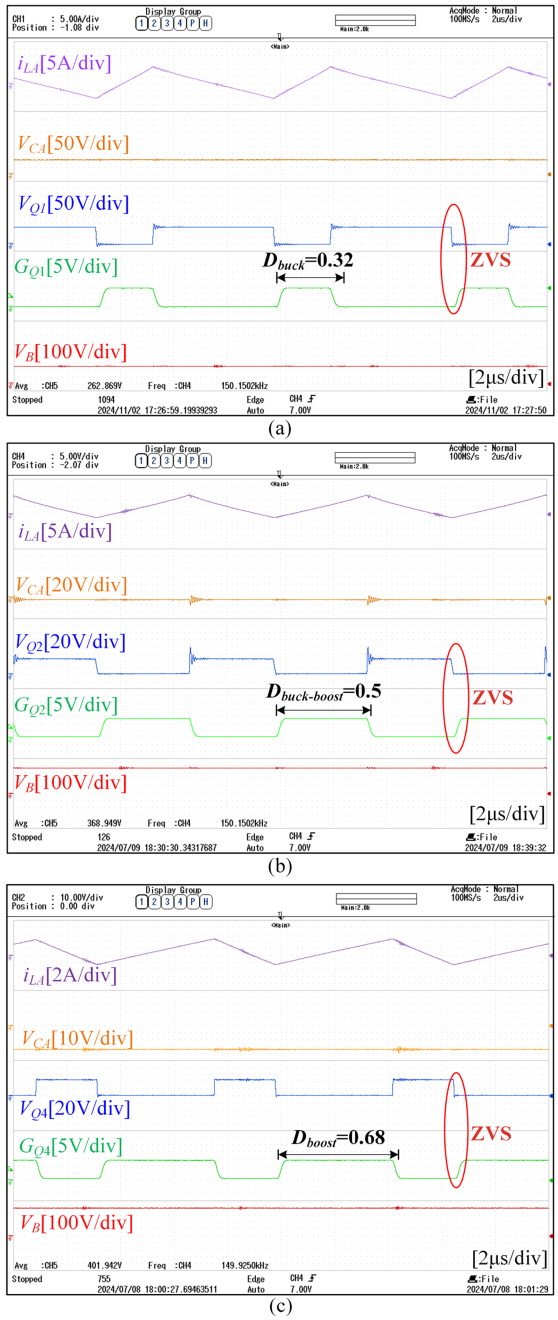

Fig. 16. Measured operating waveforms of the DC/DC converter. (a) Buck mode. (b) Buck-boost mode. (c) Boost mode.

regulation voltage V_R of 16 V. Notably, throughout the whole battery charging process, V_H is consistently maintained at a constant voltage of 418 V, demonstrating that V_H, V_R, and V_B are following the voltage constraints described in (4).

The key operating waveforms of the WPT stage during the CC and CV charging stages are shown in Fig. 15. From these waveforms, it can be observed that the voltage of the compensation circuit slightly leads the current and the input impedance is inductive, which enables the ZVS turn-ON of the inverter switches.

During the battery charging process, the dc/dc converter seamlessly transitions between buck, buck-boost, and boost modes according to the control diagram. The critical waveforms for these three modes are illustrated in Fig. 16. In Fig. 16(a), the converter operates in buck mode with the duty cycle (D_{buck}) of 0.32 and a power ratio δ value of approximately 0.37. Fig. 16(b) showcases the converter operating in buck-boost mode with a duty cycle (D_{bb}) of 0.5 and δ is about 0.12. Fig. 16(c) illustrates the converter operating in boost mode with a duty cycle (D_{boost}) of 0.68, and δ is about 0.038. Throughout the whole charging process, the dc/dc converter consistently operates in DCM, enabling ZVS turn-ON to ensure high efficiency.

B. Operating Transient Waveforms of Mode Switching

To facilitate a wide output range with high efficiency, the dc/dc converter incorporates three operational modes to meet varying voltage gain requirements during different stages of battery charging. However, to ensure continuous and stable charging, it is imperative for the converter to transition between these operating modes.

The operating transient waveforms of the dc/dc converter switching between three operating modes are shown in Fig. 17. Fig. 17(a) shows the operating transient waveforms during the transition from buck mode to buck-boost mode during the CC charging stage, with a load step change in R_B from 111 Ω to 123 Ω. Upon detecting the load change, the controller initiates the mode switching process and adjusts the duty cycle of Q_4

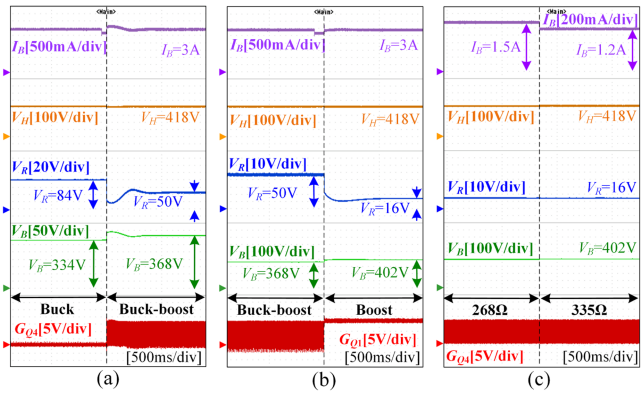

Fig. 17. Measured operating transient waveforms. (a) Buck to buck-boost. (b) Buck-boost to boost. (c) R_B Step from 268 to 335 Ω in boost mode.

from 0 to D. Before and following the step change, V_H remains constant while V_B transitions from 334 to 368 V. Fig. 17(b) shows the operating transient waveforms of buck-boost mode to boost mode during the CC charging stage, where R_B is stepped up from 123 to 131 Ω. Upon detecting the load change, the controller enters into a switching process and modifies the duty cycle of Q_1 from D to 1. Similarly, V_H remains constant while V_B undergoes a change from 368 to 402 V. Fig. 17(c) demonstrates the waveforms during the CV charging stage with the converter operating in boost mode. The value of R_B changes from 268 to 335 Ω, and both V_H and V_B remain stable throughout this process. These operating transient waveforms clearly demonstrate that the proposed NP-PPC WCS achieves transitions between the three operating modes (buck, buck-boost, and boost) during the battery charging process.

C. System Efficiency Analysis

To provide a fair efficiency comparison, an experimental prototype of a conventional PPC WCS with the same charging specifications was constructed. The efficiency comparison among the proposed NP-PPC WCS, the conventional PPC WCS, and the conventional two-stage WCS, measured throughout the charging process, as shown in Fig. 18.

From Fig. 18, it is evident that during the initial charging stage, the power ratio δ of the conventional PPC WCS is lower than that of the proposed NP-PPC WCS, resulting in higher efficiency in this stage. As charging progresses, the δ value decreases for the proposed NP-PPC WCS while increasing for conventional PPC WCS, leading to higher efficiency for the proposed NP-PPC WCS after V_{B1}. The efficiency curves in Fig. 18(a) show that NP-PPC achieves a 2% higher $\eta_{\max}$ compared to the conventional PPC WCS due to the lower $\delta_{\min}$ value for the proposed NP-PPC WCS. As the CV charging stage progresses, the charging power decreases, leading to a light-load operating condition in the dc/dc converter and a subsequent decrease in system efficiency. However, due to the significantly lower δ value of the proposed NP-PPC WCS compared to the conventional PPC WCS, the efficiency of the proposed NP-PPC WCS is less affected by light-load conditions than that of the conventional PPC WCS. The efficiency difference amounted to 11.94% until the charging

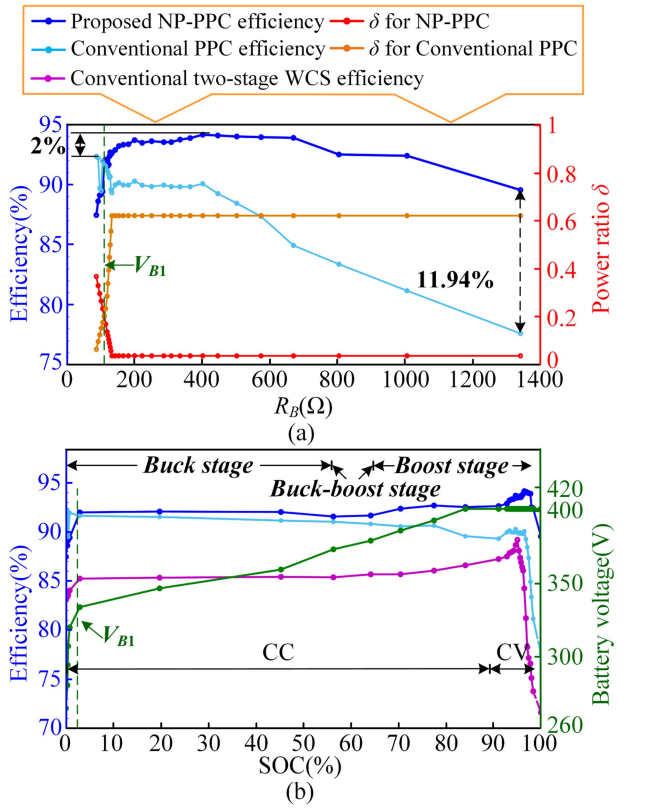

Fig. 18. Measured system efficiency of the proposed three-coil NP-PPC WCS, the conventional PPC WCS, and the conventional two-stage WCS versus (a) R_B and (b) SOC.

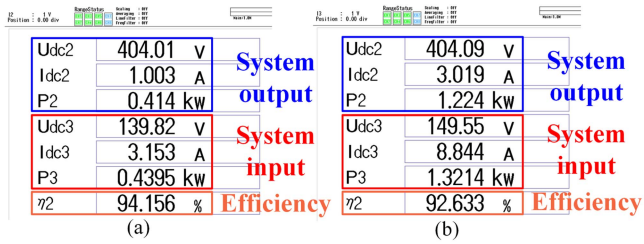

Fig. 19. Screen capture of experimental power analyses. (a) Maximum efficiency. (b) Maximum power point efficiency.

was completed. These findings demonstrate that NP-PPC can tolerate less efficient dc/dc converters while maintaining better compatibility in practical applications compared with the conventional PPC WCS. Furthermore, an experimental test of the conventional two-stage WCS was also conducted, revealing that the NP-PPC and the conventional PPC structures exhibit higher efficiency throughout the overall charging cycle compared to the conventional two-stage WCS structure. This conclusion is further supported by Xiong et al. [24] and Wang et al. [25].

To visually demonstrate the comparative efficiency of the charging process, Fig. 18(b) presents efficiency comparison curves with SOC as the axis after scaling up. The superiority of the proposed NP-PPC WCS over the conventional PPC WCS in terms of efficiency is consistently observed when the battery voltage exceeds V_{B1}. By combining Figs. 18 and 19, it can be

TABLE VI
COMPARISONS OF COIL NUMBER, REGULATION RANGE, AND EFFICIENCY

Reference	Need DC/DC	Number of coils	Charging profile	Wireless feedback	Output power	Output voltage	Power ratio range	Efficiency	Regulation power
Luo et al. [29]	No	2	Constant Power (CP)	Yes	3 kW	——	——	87.5–91.5%	Full
Jiang et al. [30]	No	2	CC/CV	Yes	0.028–0.28 kW	32–72 V	——	60–90.2%	Full
Kim et al. [31]	Yes	2	CC/CV	Yes	0.4–3.4 kW	240–410 V	——	75–89.6%	Full
Wang et al. [23]	Yes	4	CC/CV	No	0.32–1.5 kW	280–320 V	0.07–0.21	83–93.6%	Partial
Xiong et al. [24]	Yes	4	CC/CV	No	0.054–0.25 kW	60–84 V	0.1–0.45	79–89%	Partial
Wang et al. [25]	Yes	4	CC/CV	No	0.21–0.43 kW	36–72 V	0.11–0.7	88–93%	Partial
This article	**Yes**	**3**	**CC/CV**	**No**	**0.12–1.2 kW**	**264–402 V**	**0.038–0.36**	**87.5–94.16%**	**Partial**

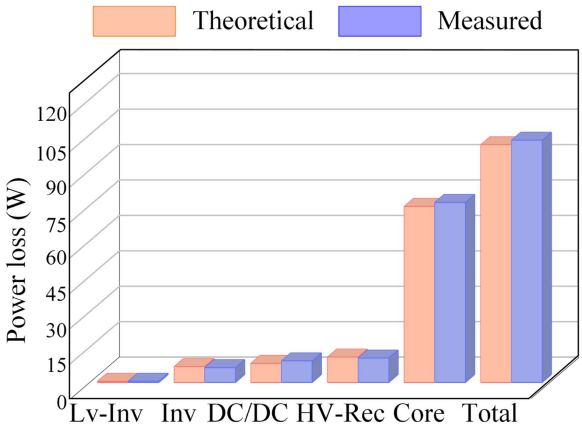

Fig. 20. Power loss of each component.

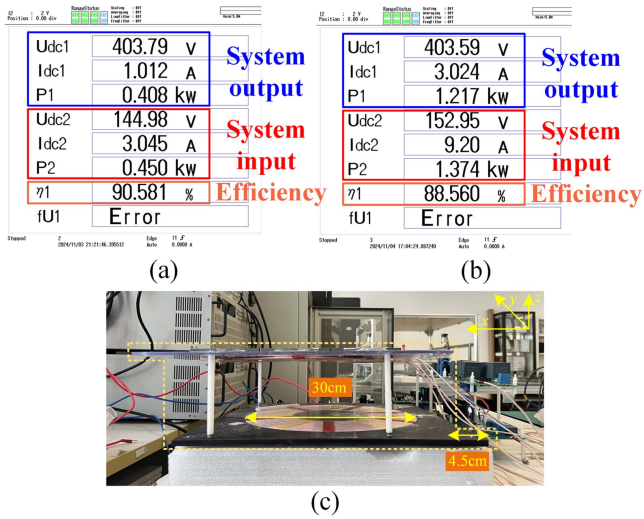

Fig. 21. Measured efficiency of the three-coil NP-PPC WCS at 15% misalignment for x- or y–direction. (a) Screen capture of the maximum efficiency point. (b) Screen capture of the maximum power point. (c) Misaligned photograph.

observed that throughout most of the charging process, the proposed NP-PPC WCS outperforms its conventional PPC WCS in terms of efficiency, achieving a peak efficiency of 94.156% [see Fig. 19(a)], a maximum power point efficiency of 92.633% [see Fig. 19(b)], and overall charging process efficiency exceeding 87%. These results highlight the significant advantages in terms of system efficiency.

Take the maximum power condition as an example. In this case, where $R_{\mathrm{ds(on)}} = 26\,\mathrm{m\Omega}$, $R_P = 410\,\mathrm{m\Omega}$, $R_{S1} = 300\,\mathrm{m\Omega}$, $R_{S2} = 45\,\mathrm{m\Omega}$, $P_{\mathrm{cv},\,P} = 25\,\mathrm{kW/m^3}$, $P_{\mathrm{cv},\,S} = 11\,\mathrm{kW/m^3}$, $P_{\mathrm{cv},LA} = 450\,\mathrm{kW/m^3}$, $V_{e,P} = V_{e,S} = 4.5 \times 10^{-4}\,\mathrm{m^3}$, while $V_{e,LA} = 1.765 \times 10^{-5}\,\mathrm{m^3}$ and $V_f = 1.8\,\mathrm{V}$. The power loss distribution according to Table II under maximum power condition is shown in Fig. 20, where the total theoretical power loss of 100.7 W is consistent with the measured power loss of 102.6 W.

D. Comparison With Previous Works

Table VI gives a comparison of the proposed three-coil NP-PPC WCS and the previous works. The key parameters, including dc/dc requirement, coil number, charging profile, regulation range, feedback, power ratio range, efficiency and power regulation mode are summarized. It demonstrates clear benefits of the proposal for wireless charging applications compared to the conventional two-stage and PPC structures in terms of coil number, regulation range (power and voltage) and efficiency.

E. Misalignment Tolerance

Conventional PPC systems typically employ four coils (two groups of rectangle and bipolar coils) with fixed-position decoupling designs [23], [24]. These systems are inherently vulnerable to misalignment issues, as any deviation from perfect alignment disrupts the decoupling state and creates unwanted coupling between power paths. In contrast, our proposed three-coil topology achieves two noncross-interfering power paths without requiring complex decoupling designs. This idea not only reduces the

number of coils but also provides inherent tolerance to misalignment issues.

While our system is primarily designed for static wireless charging scenarios where precise positioning can be achieved through standard EV positioning systems, we have evaluated its performance under the misalignment condition. The measured efficiency under 15% misalignment for x or y direction is presented in Fig. 21. The system obtains a maximum efficiency of 90.581% and an efficiency of 88.56% at the maximum power point. The results confirm that the proposed design can tolerate the practical misalignment challenges while maintaining high efficiency levels.

VI Conclusion

This article proposes a novel three-coil NP-PPC WCS, which enables a wide output range while maintaining high efficiency. The proposed NP-PPC concept inverts the voltage polarity of the regulation converter, allowing a higher proportion of unregulated power transfer compared to conventional PPC systems. Through circuit analysis, two independent power paths are obtained using only three coils, eliminating the need for additional decoupling and enhancing system compactness. A comprehensive control strategy is devised to facilitate CC-CV battery charging and hysteresis control switching between buck, buck-boost, and boost modes without relying on wireless communication. Experimental validation of a 500 W prototype demonstrates the superiority of the proposed NP-PPC WCS over conventional PPC WCS in terms of efficiency. The proposed NP-PPC WCS achieves a peak efficiency of 94.156%, outperforming conventional PPC for over 95% of the charging process, with a maximum efficiency increase of 2% and a light load efficiency increase of 11.94%.

References

[1] T. Imura and Y. Hori, "Maximizing air gap and efficiency of magnetic resonant coupling for wireless power transfer using equivalent circuit and Neumann formula," *IEEE Trans. Ind. Electron.*, vol. 58, no. 10, pp. 4746–4752, Oct. 2011.

[2] C. Duan, C. Jiang, A. Taylor, and K. Bai, "Design of a zero-voltage switching large-air-gap wireless charger with low electrical stress for Plugin hybrid electric vehicles," in *Proc. IEEE Transp. Electrific. Conf. Expo*, Jun. 2013, pp. 1–5.

[3] A. Khaligh and M. D'Antonio, "Global trends in high-power on-board chargers for electric vehicles," *IEEE Trans. Veh. Technol.*, vol. 68, no. 4, pp. 3306–3324, Apr. 2019.

[4] G. A. Covic and J. T. Boys, "Inductive power transfer," *Proc. IEEE*, vol. 101, no. 6, pp. 1276–1289, Jun. 2013.

[5] B. Zou and Z. Huang, "Primary-frequency-tuning and secondary-impedance-matching IPT converter with programmable constant power output and optimal efficiency tracking against variation of coupling coefficient," *IEEE Trans. Power Electron.*, vol. 39, no. 4, pp. 4895–4909, Apr. 2024.

[6] C. Jung, "Power up with 800–V systems: The benefits of upgrading voltage power for battery–electric passenger vehicles," *IEEE Electrific. Mag.*, vol. 5, no. 1, pp. 53–58, Mar. 2017.

[7] V. Ramakrishnan et al., "A comprehensive review on efficiency enhancement of wireless charging system for the electric vehicles applications," *IEEE Access*, vol. 12, pp. 46967–46994, 2024.

[8] A. Al-Haj Hussein and I. Batarseh, "A review of charging algorithms for nickel and lithium battery chargers," *IEEE Trans. Veh. Technol.*, vol. 60, no. 3, pp. 830–838, Mar. 2011.

[9] I.-W. Iam et al., "Constant-frequency and noncommunication-based inductive power transfer converter for battery charging," *IEEE J. Emerg. Sel. Topics Power Electron.*, vol. 10, no. 2, pp. 2147–2162, Apr. 2022.

[10] F. Xu, S.-C. Wong, and C. K. Tse, "Overall loss compensation and optimization control in single-stage inductive power transfer converter delivering constant power," *IEEE Trans. Power Electron.*, vol. 37, no. 1, pp. 1146–1158, Jan. 2022.

[11] W. Liu, K. T. Chau, C. H. T. Lee, C. Jiang, W. Han, and W. H. Lam, "A wireless dimmable lighting system using variable–power variable–frequency control," *IEEE Trans. Ind. Electron.*, vol. 67, no. 10, pp. 8392–8404, Oct. 2020.

[12] X. Wang, J. Xu, M. Leng, H. Ma, and S. He, "A hybrid control strategy of LCC-S compensated WPT system for wide output voltage and ZVS range with minimized reactive current," *IEEE Trans. Ind. Electron.*, vol. 68, no. 9, pp. 7908–7920, Sep. 2021.

[13] I.-W. Iam, Z. Ding, C.-F. Ieong, C.-S. Lam, R. P. Martins, and P.-I. Mak, "Optimal bivariate control strategy of multi-stage constant current charging for ipt-based wireless electric vehicle charging," *IEEE Trans. Transp. Electrific.*, vol. 1, no. 1, pp. 4513–4528, Aug. 2023.

[14] Y. Zhang, Z. Shen, W. Pan, H. Wang, Y. Wu, and X. Mao, "Constant current and constant voltage charging of wireless power transfer system based on three-coil structure," *IEEE Trans. Ind. Electron.*, vol. 70, no. 1, pp. 1066–1070, Jan. 2023.

[15] M. Debbou and F. Colet, "Inductive wireless power transfer for electric vehicle dynamic charging," in *Proc. IEEE PELS Workshop Emerg. Technol., Wireless Power Transfer*, Oct. 2016, pp. 118–122.

[16] J. H. R. Enslin and D. B. Snyman, "Combined low-cost, high-efficient inverter, peak power tracker and regulator for PV applications," *IEEE Trans. Power Electron.*, vol. 6, no. 1, pp. 73–82, Jan. 1991.

[17] A. Nabinejad, A. Rajaei, and M. Mardaneh, "A systematic approach to extract state-space averaged equations and small-signal model of partial-power converters," *IEEE J. Emerg. Sel. Topics Power Electron.*, vol. 8, no. 3, pp. 2475–2483, Sep. 2020.

[18] J. W. Zapata, S. Kouro, G. Carrasco, H. Renaudineau, and T. A. Meynard, "Analysis of partial power DC–DC converters for two-stage photovoltaic systems," *IEEE J. Emerg. Sel. Topics Power Electron.*, vol. 7, no. 1, pp. 591–603, Mar. 2019.

[19] H. Zhou, J. Zhao, and Y. Han, "PV balancers: Concept, architectures, and realization," *IEEE Trans. Power Electron.*, vol. 30, no. 7, pp. 3479–3487, Jul. 2015.

[20] N. Kim and B. Parkhideh, "PV-battery series inverter architecture: A solar inverter for seamless battery integration with partial-power DC–DC optimizer," *IEEE Trans. Energy Convers.*, vol. 34, no. 1, pp. 478–485, Mar. 2019.

[21] M. C. Mira, Z. Zhang, K. L. Jørgensen, and M. A. E. Andersen, "Fractional charging converter with high efficiency and low cost for electrochemical energy storage devices," *IEEE Trans. Ind. Appl.*, vol. 55, no. 6, pp. 7461–7470, Nov./Dec. 2019.

[22] G. Fan, X. Wu, T. Liu, and Y. Xu, "High-efficiency high-density MHz cellular DC/DC converter for on-board charger," *IEEE Trans. Power Electron.*, vol. 37, no. 12, pp. 15666–15677, Dec. 2022.

[23] X. Wang, J. Xu, H. Ma, and P. Yang, "A high efficiency LCC-S compensated WPT system with dual decoupled receive coils and cascaded PWM regulator," *IEEE Trans. Circuits Syst. II*, vol. 67, no. 12, pp. 3142–3146, Dec. 2020.

[24] W. Xiong, Z. Yan, D. Tang, W. Zhou, and R. Mai, "A hybrid topology IPT system with partial power processing for CC-CV charging," *IEEE Trans. Power Electron.*, vol. 39, no. 1, pp. 1701–1712, Jan. 2024.

[25] X. Wang, L. He, J. Xu, C. -K. Lee, and C. K. Tse, "Power–spilt–based wireless charging system with communication–free coordination control," *IEEE Trans. Power Electron.*, vol. 38, no. 2, pp. 2754–2767, Feb. 2023.

[26] S. Liu et al., "Efficiency improvement of dual-receiver WPT systems based on partial power processing control," *IEEE Trans. Power Electron.*, vol. 37, no. 6, pp. 7456–7469, Jun. 2022.

[27] *Electric Vehicle Wireless Power Transfer (WPT) Systems– Part 1: General requirements*, IEC 61980-1:2020, Geneva, Switzerland: Int. Electrotech. Commission, 2020. [Online]. Available: https://webstore.iec.ch/en/publication/31657

[28] *Wireless Power Transfer For Light Duty Plug-In/Electric Vehicles and Alignment Methodology*, SAE J2954_201904, Pittsburgh, PA, USA: SAE Int., 2019. [Online]. Available: https://www.sae.org/publications/technical-papers/content/j2954_201904/

[29] Z. Luo, Y. Zhao, M. Xiong, X. Wei, and H. Dai, "A self-tuning LCC/LCC system based on switch-controlled capacitors for constant-power wireless electric vehicle charging," *IEEE Trans. Ind. Electron.*, vol. 70, no. 1, pp. 709–720, Jan. 2023.

[30] Y. Jiang et al., "Phase-locked loop combined with chained trigger mode used for impedance matching in wireless high power transfer," *IEEE Trans. Power Electron.*, vol. 35, no. 4, pp. 4272–4285, Apr. 2020.

[31] M. Kim, D.-M. Joo, and B. K. Lee, "Design and control of inductive power transfer system for electric vehicles considering wide variation of output voltage and coupling coefficient," *IEEE Trans. Power Electron.*, vol. 34, no. 2, pp. 1197–1208, Feb. 2019.

Muxing Wu (Graduate Student Member, IEEE) received the B.Sc. degree in electrical and intelligent engineering from Xiangtan University, Xiangtan, China, in 2018, and the M.Sc. degree in electrical engineering from Yanshan University, Qinhuangdao, China, in 2022. He is currently working toward the Ph.D. degree in electrical and computer engineering with the University of Macau (UM), Macau, China.

His current research interests include wireless power transfer and resonant converter.

Io-Wa Iam received the B.Sc. and Ph.D. degrees in electrical and computer engineering from the University of Macau (UM), Macau, China, in 2020 and 2023, respectively.

He is currently a Research Assistant Professor with the State Key Laboratory of Analog and Mixed-Signal VLSI and the Institute of Microelectronics, UM. His current research interests include power electronics and wireless power transfer.

Dr. Iam was the recipient of the Macao Science and Technology R&D Award for Postgraduates (Ph.D. Level) in 2024. In 2019, he was awarded the "Best Track Paper Award" in APPEEC 2019.

Chi-Seng Lam (Senior Member, IEEE) received the Ph.D. degree in electrical and electronics engineering from the University of Macau (UM), Macau, China, in 2012. He completed the Clare Hall Study Programme from the University of Cambridge, Cambridge, U.K., in 2019.

In 2013, he was a Postdoctoral Fellow with The Hong Kong Polytechnic University, Hong Kong, China. He is currently an Associate Professor with the State Key Laboratory of Analog and Mixed-Signal VLSI and the Institute of Microelectronics, UM, and also with the Department of Electrical and Computer Engineering, Faculty of Science and Technology, UM. He has coauthored or co-edited five books and more than 200 technical journals and conference papers. He holds six U.S. and seven Chinese patents. His research interests include power quality compensators, photovoltaic energy generation system, power management integrated circuits, and wireless power transfer.

Dr. Lam was the recipient or co-recipient of the IEEE PES Chapter Outstanding Engineer Award in 2016, the Gold Medal of the 48th Geneva International Exhibition of Inventions in 2023, and the Macao Science and Technology Invention Awards (Third Class, Second Class and Third Class) in 2014, 2018, and 2024, respectively. He is currently the Chair of the Young Professionals in Circuits and Systems of IEEE CASS, Founding Chair of the IEEE Macau IES Chapter, and the Secretary for IEEE IES Technical Committee on Power Electronics. He is currently an Associate Editor for IEEE TRANSACTIONS ON POWER ELECTRONICS, IEEE TRANSACTIONS ON INDUSTRIAL ELECTRONICS, IEEE JOURNAL OF EMERGING AND SELECTED TOPICS IN POWER ELECTRONICS, IEEE OPEN JOURNAL OF THE INDUSTRIAL ELECTRONICS SOCIETY, and IEEE ACCESS. He was the recipient of the 2021 IEEE Access Outstanding Associate Editor, and the 2022 IEEE Transactions on Industrial Electronics Distinguished Reviewer, and the 2024 IEEE TRANSACTIONS ON POWER ELECTRONICS Outstanding Reviewer.